energies

MDPI

Article

Rapid Optimization Method for Grid-Forming Energy Storage Systems Frequency Control Based on Leader–Follower Game Strategy

Yingjun Guo [1], Yu Qi [1], Chunxiao Mei [2], Yanxun Guo [3], Erhui Zhang [4], Shuo Zhang [3] and Hexu Sun [1,*]

[1] School of Electrical Engineering, Hebei University of Science and Technology, Shijiazhuang 050018, China; guoyj@hebust.edu.cn (Y.G.)
[2] Hebei Province Construction & Investment Group Co., Ltd., Shijiazhuang 050000, China
[3] Suntien Green Energy Co., Ltd., Shijiazhuang 050000, China
[4] HeBei Suntien New Energy Technology Co., Ltd., Zhangjiakou 075000, China
* Correspondence: hxsun@hebust.edu.cn

Abstract

The integration of grid-forming energy storage systems (GFM-ESSs) provides essential support for the stable operation of grid-connected converters in renewable energy systems. However, GFM-ESSs may exhibit low-frequency oscillations in response to grid state variations, posing a threat to power system stability. To address this challenge, this paper proposes a fast continuous optimization method for the active power–frequency control loop of multi-VSG-based GFM-ESSs. First, a parameter coupling model for multiple VSGs is established, and an internal parameter decoupling control strategy is proposed. Subsequently, an iterative optimization model based on a gradient-based master–slave game is developed, in which the minimization of converter frequency deviation serves as the leader's objective, while the minimization of system frequency deviation acts as the follower's objective. Frequency fluctuations are further mitigated through tracking differentiator-based active power compensation. The effectiveness of the proposed method is validated through simulation with six GFM-ESS units integrated into a modified IEEE 33-node system featuring six renewable energy stations. Simulation results demonstrate that the proposed approach significantly suppresses frequency fluctuations while also reducing the response time and the rate of frequency change under grid disturbance conditions.

Keywords: grid-forming energy storage system; frequency optimization; gradient-based leader–follower game; multi-machine operation

Check for updates

Academic Editor: José Matas

Received: 31 March 2026
Revised: 1 May 2026
Accepted: 13 May 2026
Published: 17 May 2026

1. Introduction

The ongoing global shift towards sustainable energy is intensifying the integration of intermittent renewable sources, such as wind and photovoltaic power, into distribution networks [1,2]. Due to the intermittent nature of renewable energy generation, voltage and frequency fluctuations in power systems have become an increasingly prominent issue [3–5]. Although traditional control methods can be effective in certain situations, they are limited by equipment capacity and response speed, making it difficult to effectively address the complex grid environment resulting from the integration of large-scale distributed energy sources [6,7]. A promising countermeasure is the deployment of large-scale energy storage systems at grid-connection points, as they can effectively mitigate voltage fluctuations and enhance system stability [8,9].

Grid-forming converters (GFCs) provide inertia and frequency support to the system by simulating the operating mechanism of a synchronous generator, making them an effective solution to the aforementioned problems. Among these, virtual synchronous generator (VSG) control has become one of the most representative control strategies in GFC due to its clear physical concept and excellent control performance [10,11]. By emulating the inertia and droop characteristics of conventional synchronous generators, VSG control facilitates dynamic regulation of both active and reactive power [12]. Typically deployed in hybrid systems combining renewable generation and energy storage, the converter is termed a Grid-Forming energy storage system (GFM-ESS) when renewable sources are disconnected. The rapid frequency and voltage response of VSG makes it well-suited for adjusting output power to enhance system stability [13]. Consequently, employing VSG to control GFM-ESSs—herein referred to as "energy storage VSG"—represents a promising and timely research direction [14].

A critical challenge, however, is that VSG-based GFCs typically exhibit low output impedance, which leads to power coupling issues during multi-VSG operation and causes imbalances between actual and reference power. This challenge has spurred research into various multi-VSG operational modes. For instance, while the area-equivalent method [15] fails to fully capture input dynamics, the linear circuit equivalent model [16] proves unsuitable for parallel VSG configurations. Ref. [17] developed a linearized model of a GFC's internal voltage phase and amplitude, analyzing damping characteristics under weak grid conditions, and ref. [18] introduced an innovative approach converting GFC harmonic motion into damped vibration. Nonetheless, these studies primarily focus on active power-transmitting GFCs, leaving the characteristics and applications of GFM-ESSs—a current research hotspot—relatively unexplored. Although recent efforts have proposed autonomous impedance matching control for GFM-ESSs [19], established transient models for hybrid systems [20], and assessed stability via Lyapunov functions [21], the research landscape in this area remains nascent. Most existing works are confined to DC microgrids [22,23] or single-unit analyses, with their applicability to multi-node AC grids yet to be thoroughly validated.

Theoretically, grid-forming energy storage is recognized as a potent solution to critical challenges in modern power systems, including low short-circuit ratios, insufficient inertia, and frequency regulation issues [24]. However, GFM-ESSs and GFC still face the same issue in the realm of small-disturbance stability, namely low-frequency oscillations caused by low damping [25,26]. To date, many researchers have proposed corresponding solutions to this problem; for example, Ref. [27] proposes a synchronous phasor-based interval oscillation suppression strategy to suppress active-power low-frequency oscillations on PV interconnection lines. Ref. [28] argues that in a multi-VSG system, active power oscillations similar to those of traditional generator-motor transients are introduced into the grid; therefore, it proposes a method involving an additional power system stabilizer. Ref. [29] describes the frequency and voltage responses of VSG active and reactive power under input power reference and grid voltage/frequency disturbances, and establishes a control strategy for static virtual impedance. Ref. [30] reveals the support mechanism of GFM-ESSs for the dynamic characteristics of traditional grid-following converters in weak grid conditions and analyzes the impact of different control loops and parameters on the system's stability under small disturbances. The experimental scenarios for the aforementioned strategies are all microgrid scenarios involving single units or multiple units in parallel; their performance in distributed grid-connected scenarios remains to be verified. In summary, there is currently a lack of practical operational testing of grid-forming energy storage in complex multi-node power grids, leaving a research gap in this area. To bridge this gap, this paper investigates a method for frequency regulation via active power compensation by integrating multiple GFM-ESS units, controlled by VSGs, into multi-node distribution grids [31]. Focusing on the ability of grid-forming storage to enable active power-based frequency support, we further propose a fast, continuous optimization method based on the VSG active power–frequency control loop to counteract frequency disturbances caused by renewable energy intermittency. It is worth noting that the concept of coordination in leader–follower hierarchical games is not unique to power systems. Ref. [32] proposes a V2G scheduling and trading framework based on the leader–follower game for vehicle-grid interaction scenarios: in this framework, the electric vehicle aggregator acts as the leader to formulate pricing strategies, while individual electric vehicles act as followers to autonomously decide on charging and discharging behaviors based on utility functions; the leader optimizes its own profits by predicting the followers' optimal reaction functions. Although this work differs from the grid-forming VSG control in this paper in terms of control strategies and incorporates blockchain technology to ensure transaction reliability, its system-level three-tier coordination architecture of "grid demand—aggregator pricing—distributed energy storage response" is highly analogous to the master–slave game framework of "grid frequency deviation—central optimizer—multi-VSG power allocation" in this paper. This architectural parallelism indirectly confirms the broad applicability of the optimization framework in GFM-ESS coordinated control.

The main contributions of this paper are summarized as follows:

- A station-level grid-connection scheme for energy storage is proposed, integrating VSG-based decoupled control strategies into the small-signal modeling of Grid-Forming Battery Storage Systems (GFM-BSSs).
- A multi-VSG secondary frequency coordination framework based on a gradient-based master–slave game is introduced. By simulating the leader–follower dynamic game process, fast and continuous optimization of active power output among multiple grid-forming energy storage units is achieved.
- A global frequency deviation minimization model and a fast control branch are developed. By unifying the objective to minimize frequency deviations at all points of common coupling (PCC) and incorporating a tracking differentiator to smoothly convert optimization commands into active power compensation signals, the overall integrity and robustness of the control system are enhanced.
- Simulation tests on a modified IEEE 33-node distribution network validate the effectiveness of the proposed method in reducing frequency deviations and improving system stability.

The remainder of this paper is organized as follows:

Section 2 introduces the system architecture, including the GFM-ESS grid-connection scheme and control principles. Section 3 details the optimization model, including objective functions, constraints, and the integration of the gradient-based master–slave game with the physical controller. Section 4 presents simulation results and analysis. Section 5 concludes the paper.

2. Basic Structure of the System

The topological model of a GFM-ESS operating in conjunction with a Grid-Connected Converter (GCC) dominated by renewable energy is illustrated in Figure 1. A typical configuration involves deploying GFM-BSS at the station level near renewable energy plants [33]. Alternatively, smaller-capacity energy storage units are often integrated within microgrids [34]. Their topology model connected to the AC grid is shown in Figure 1. The main circuit portion of the diagram defines U_{bus} and E_{g}, representing the DC bus voltage and grid connection node voltage; R_{g} and X_{g} denote the line resistance and reactance; L_{f} and C_{f} denote the inductance and capacitance of the low-pass filter. Within the control loop section, P_{ref}, Q_{ref}, ω_{ref}, U_{ref} represent the reference values for active power, reactive power, frequency and voltage; P and Q denote the calculated values of active power and reactive power transmitted by the GFM-ESS to the grid; and δ and E represent the voltage phase angle and voltage magnitude of the VSG.

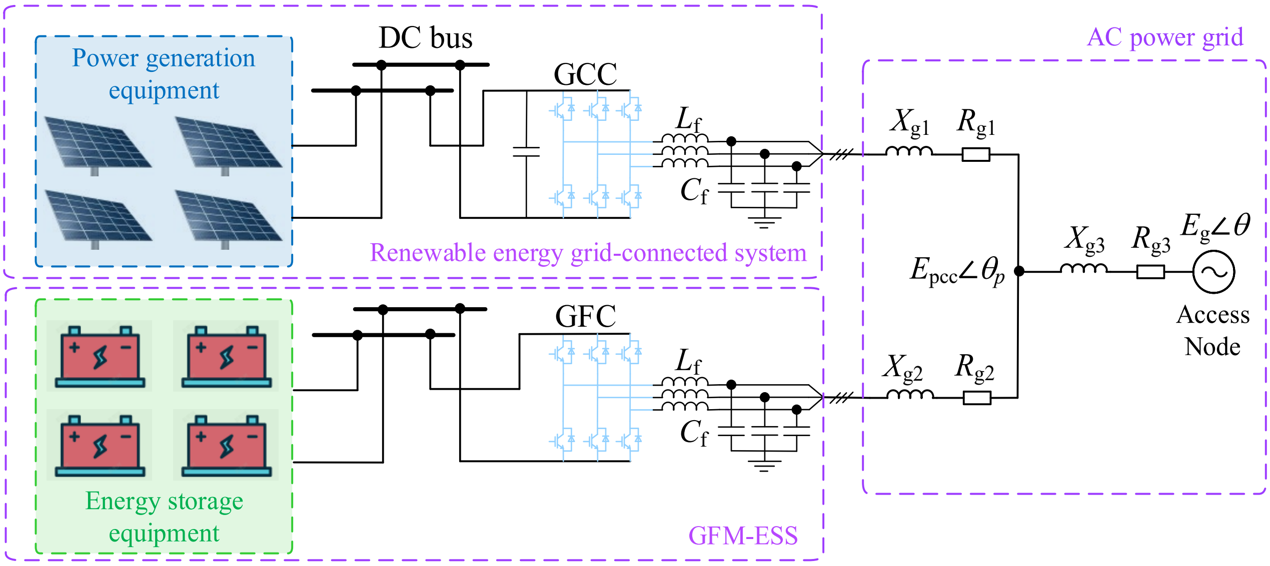

Figure 1. Topological modeling of a GFM-ESS connected to the AC grid.

2.1. Power Model of GFM-ESS

The GFM-ESS's connection to the AC grid can be physically modelled as an AC voltage source delivering power to a node. Based on the voltage phasors and line impedance phasors, the complex power of the system is calculated:

$$\tilde{S} = \frac{Ee^{j\delta}\left(Ee^{j\delta} - E_{pcc}e^{j\theta_p}\right)^*}{\sqrt{{X_{g2}}^2 + {R_{g2}}^2}e^{j\gamma}} \tag{1}$$

$$\gamma = \arctan\frac{X_{g2}}{R_{g2}} \tag{2}$$

In the equation, "*" denotes the conjugate of the phasor. Decomposing the real and imaginary parts of the complex power, the active and reactive power delivered by the GFM-ESS to the grid node are:

$$P = \frac{EE_{pcc}}{\sqrt{X_{g2}^2 + R_{g2}^2}}\sin(\delta - \theta_p + \gamma) - \frac{R_{g2}E_{pcc}^2}{X_{g2}^2 + R_{g2}^2} \tag{3}$$

$$Q = \frac{EE_{pcc}}{\sqrt{X_{g2}^2 + R_{g2}^2}}\cos(\delta - \theta_p + \gamma) - \frac{X_g E_{pcc}^2}{X_{g2}^2 + R_{g2}^2} \tag{4}$$

Take the partial derivatives of δ and E with respect to the variables in Equations (3) and (4):

$$\frac{\partial P}{\partial \delta} = \frac{EE_{pcc}}{\sqrt{X_{g2}^2 + R_{g2}^2}}\cos(\delta - \theta_p + \gamma) \tag{5}$$

$$\frac{\partial Q}{\partial E} = \frac{E_{pcc}}{\sqrt{X_{g2}^2 + R_{g2}^2}}\cos(\delta - \theta_p + \gamma) \tag{6}$$

Define the voltage angle small signal as $\Delta\delta = \delta - \theta_{\mathrm{p}}$. From Equations (5) and (6), the small-signal expression for GFM-ESS power transfer can be derived as:

$$\Delta P = \frac{EE_{\mathrm{pcc}}}{\sqrt{X_{\mathrm{g2}}^2 + R_{\mathrm{g2}}^2}}\Delta\delta \tag{7}$$

$$\Delta Q = \frac{E_{\mathrm{pcc}}}{\sqrt{X_{\mathrm{g2}}^2 + R_{\mathrm{g2}}^2}}\Delta E \tag{8}$$

In the equation, Δ• represents the variable. "•" corresponds to the small-signal component.

2.2. Power Coupling to Voltage Phase Angle and Voltage Amplitude

According to Equations (3)–(8), the small-signal active power can be directly represented by the small-signal voltage angle. Similarly, the small-signal reactive power can be directly represented by the small-signal voltage. By the same token, we need to investigate the coupling of active power to the voltage magnitude and the coupling of reactive power to the voltage angle. Take the partial derivatives of E and δ in Equations (3) and (4):

$$\frac{\partial P}{\partial E} = \frac{E_{\mathrm{pcc}}}{\sqrt{X_{\mathrm{g2}}^2 + R_{\mathrm{g2}}^2}}\sin(\delta - \theta_{\mathrm{p}} + \gamma) \tag{9}$$

$$\frac{\partial Q}{\partial \delta} = -\frac{EE_{\mathrm{pcc}}}{\sqrt{X_{\mathrm{g2}}^2 + R_{\mathrm{g2}}^2}}\sin(\delta - \theta_{\mathrm{p}} + \gamma) \tag{10}$$

Similarly, transforming the above partial derivative expression into small-signal form:

$$\Delta P = \frac{E_{\mathrm{pcc}}\sin(\delta_0 + \gamma)}{\sqrt{X_{\mathrm{g2}}^2 + R_{\mathrm{g2}}^2}}\Delta E \tag{11}$$

$$\Delta Q = -\frac{EE_{\mathrm{pcc}}}{\sqrt{X_{\mathrm{g2}}^2 + R_{\mathrm{g2}}^2}}\sin(\Delta\delta + \gamma) \tag{12}$$

In the equation, δ_0 represents the initial value of the voltage angle. It may be noted that the voltage angle small-signal and reactive power small-signal exhibit a sinusoidal relationship, implying that a static bias always exists causing reactive power displacement.

2.3. Control Principle and Parameter Decoupling Model of VSG

VSG control is a grid-connection control method developed by modelling the rotor and stator equations of synchronous generators. The grid-forming power angle is established based on the second-order rotor equations of synchronous machines, while the grid-forming voltage is established based on the stator equations of synchronous machines [35]. The grid-forming power angle equation in VSG control is:

$$\begin{cases} \frac{\mathrm{d}\delta}{\mathrm{d}t} = \omega - \omega_{\mathrm{ref}} \\ J\frac{\mathrm{d}\omega}{\mathrm{d}t} = \frac{P_{\mathrm{ref}} - P}{\omega_{\mathrm{ref}}} - D(\omega - \omega_{\mathrm{ref}}) \end{cases} \tag{13}$$

The relationship between the reactive power and voltage of the VSG exhibits droop characteristics. However, the rotor motion of the VSG introduces inertia characteristics to the stator. Consequently, the grid voltage equation is:

$$E = U_{\mathrm{ref}} + \frac{1}{K_{\mathrm{qu}}(Js + D)}(Q_{\mathrm{ref}} - Q) \tag{14}$$

According to (13) and (14), when the system is in steady state, the carrier component of the GFM-ESS output voltage is expressed as:

$$U_{\mathrm{n}}(t) = E\sin(\omega_{\mathrm{ref}}t + \delta) \tag{15}$$

At this point, the power electronic converter generates a pulse width modulated waveform with equivalent area.

Within the VSG system, frequency fluctuations not only affect the dynamic response of the power grid but are also fed back into the voltage regulation mechanism via the VSG's control strategy. Combining Equations (7) and (8), the feedback relationship between the voltage angle and voltage pair in the VSG system with respect to active and reactive power is illustrated in Figure 2.

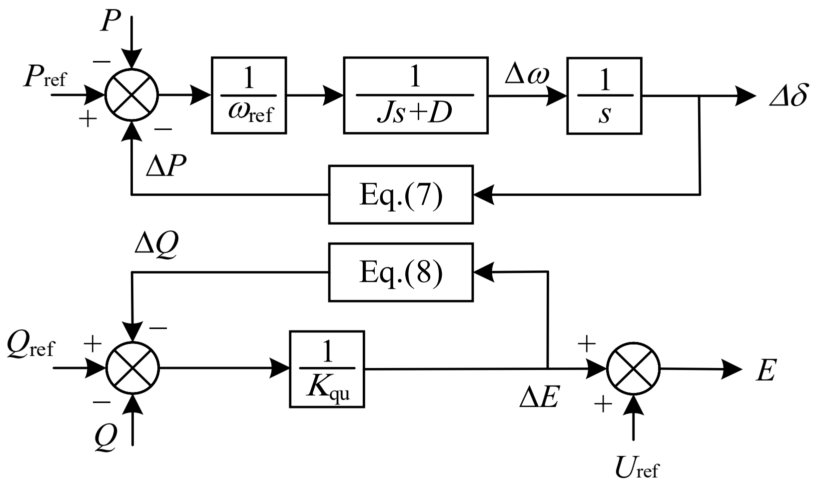

Figure 2. Feedback relationship between voltage angle and voltage on active and reactive power.

In VSG systems, inherent power coupling exists between active power and voltage magnitude, as well as between reactive power and power angle [36]. This coupling adversely affects the dynamic performance and stability of multi-VSG systems, particularly during transient events where it introduces harmful oscillations and complicates control coordination [37]. To mitigate this issue and establish a clear foundation for subsequent multi-VSG optimization, this paper proposes an internal parameter decoupling control strategy. The core objective of this strategy is to minimize cross-coupling effects by ensuring the active power loop primarily responds to power angle/frequency deviations, while the reactive power loop primarily responds to voltage magnitude deviations.

We achieve this by introducing decoupling compensators into the VSG control structure. Based on the small-signal coupling relationship defined by Equations (11) and (12), compensation signals are generated and injected into the corresponding control loops. Figure 3 illustrates the proposed decoupling control structure.

This decoupling strategy effectively linearizes and diagonalizes the power control input-output relationship of the VSG near the operating point. It simplifies the dynamic characteristics of multi-VSG systems, making them more amenable to advanced coordination strategies such as the leader–follower game proposed in Section 3.

2.4. Grid-Connection Control Method for New Energy Equipment

The new energy equipment connects to the GCC via the DC bus, employing a conventional grid-following control strategy for grid connection. The grid-connected voltage is determined by the outer power loop and inner current loop; the voltage angle is calculated by sampling the PCC voltage through a phase-locked loop (PLL), as illustrated in Figure 4.

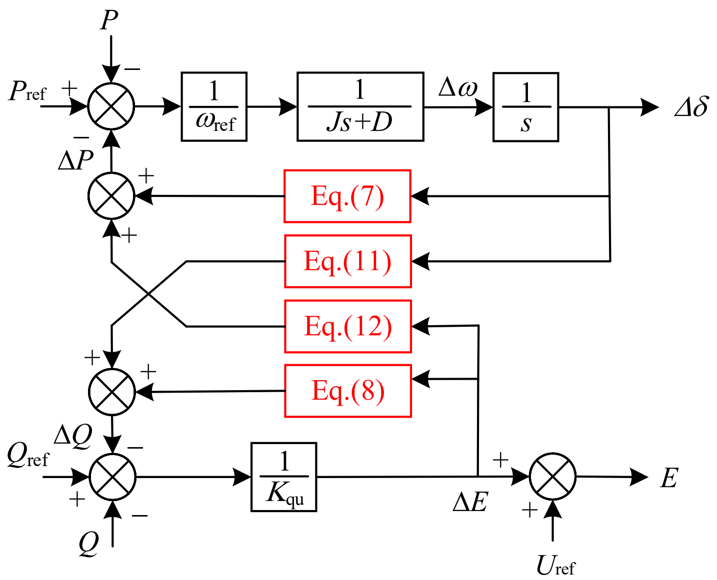

Figure 3. Power coupling relationship between voltage angle and voltage.

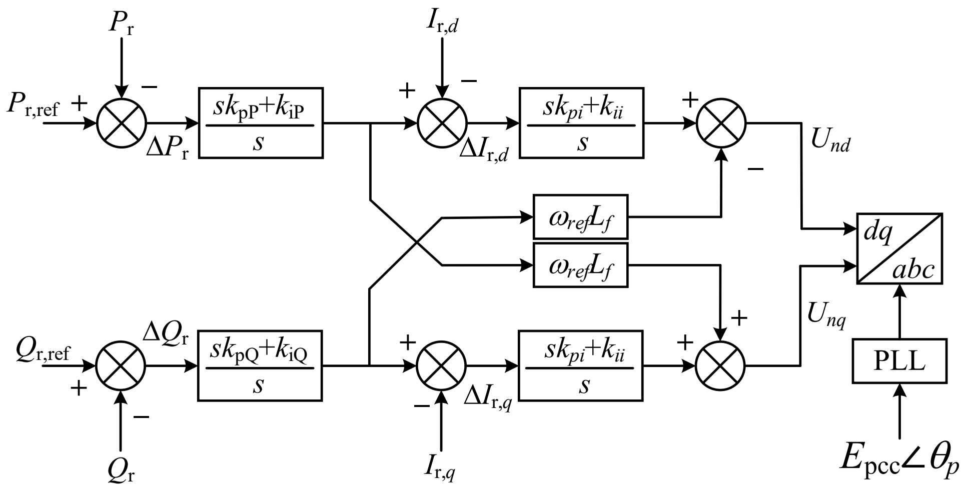

Figure 4. Voltage control of new energy equipment.

In Figure 4, $P_{\mathrm{r,ref}}$ and $Q_{\mathrm{r,ref}}$ denote the reference active and reactive power of the GCC respectively; P_{r} and Q_{r} represent the sensed active and reactive power of the GCC; $I_{\mathrm{r},d}$ and $I_{\mathrm{r},q}$ denote the d-axis and q-axis components of the GCC output current respectively; U_{nd} and U_{nq} are the modulated wave outputs of the GCC controller. The control parameters for GCC are defined as follows: k_{pP} and k_{iP} denote the proportional and integral gains of the active power outer loop, respectively; k_{pQ} and k_{iQ} denote the proportional and integral parameters of the reactive power outer loop respectively; and k_{pi} and k_{ii} denote the proportional and integral parameters of the current inner loop respectively. Additionally, a PI loop exists within the PLL, with its parameters defined as $k_{\mathrm{p,pll}}$ and $k_{\mathrm{i,pll}}$.

3. Establishment of Short-Term Optimization Models

To define the scope of this study and focus on its core contributions, the proposed optimization control method is established under the following fundamental assumptions:

Assumption 1: *The communication network linking the upper-level optimizer and the local controllers of the VSG units is assumed to have negligible latency and be free of packet loss, thereby ensuring real-time exchange of optimization commands and state information.*

Assumption 2: *Within each short-term optimization time window, variations in renewable generation and load are considered slow relative to the system's electromechanical transient dynamics. Consequently, the operating point can be approximated as quasi-steady-state, permitting the use of a combined algebraic-differential equation model for optimization calculations.*

Assumption 3: *The dynamic response of the inner power-tracking control loops of each VSG is assumed to be substantially faster than the upper-level optimization cycle. Hence, the local controllers are modeled as ideal actuators capable of executing the dispatched active power adjustment commands without tracking error.*

Assumption 4: *The necessary system information—including grid topology, line impedances, and VSG control parameters—is assumed to be known a priori and remain constant throughout the optimization horizon.*

3.1. Objective Function and Constraints

Short-term optimization models employ small time steps; however, overly intricate modeling can increase computational costs. The optimization model comprises an objective function and constraints. This study aims to minimize the frequency deviation across all PCCs within the distribution network to enhance system frequency stability. Consequently, the root mean square (RMS) of frequency deviations at all monitored nodes is adopted as the objective function:

$$f = \sqrt{\frac{1}{m}\sum_{i=1}^{m}(\omega_i - \omega_{\mathrm{ref}})^2} \tag{16}$$

Here, m denotes the number of nodes of interest within the distribution substation, representing the frequency deviation of the i-th node. When considering continuous optimization over short time scales, the objective function may be defined as the average of the root mean square of frequency deviations within the optimization time window:

$$f^{\alpha} = \frac{1}{\alpha}\sum_{t=1}^{\alpha}\left[\sqrt{\frac{1}{m}\sum_{i=1}^{m}(\omega_i - \omega_{\mathrm{ref}})^2}\right] \tag{17}$$

In the formula, α represents the optimization time step, which is a quantity exceeding ten times the sampling time step. The optimization objective of this paper is to minimize frequency deviation within a given time series while ensuring the safe operation of the energy storage VSG during charging and discharging processes, satisfying constraints on energy storage capacity and charge/discharge power.

In the VSG energy storage system, power constraints apply to both charging and discharging operations. The power constraints for source-side energy storage devices are as follows:

$$P_{ess,j}^{\min} \le P_{ess,j} \le P_{ess,j}^{\max} \tag{18}$$

In the equation, P_{ess} denotes the output power of the energy storage device; the subscript j represents the device number, with an upper limit of n energy storage devices; the superscripts min and max denote the minimum and maximum values respectively. The energy storage devices are connected to the DC bus, which also imposes a power constraint on the converter, namely:

$$\sum_{j=1}^{n} P_{ess,j}^{\min} \le \sqrt{P_{ref}^2 + Q_{ref}^2} \le \sum_{j=1}^{n} P_{ess,j}^{\max} \tag{19}$$

The upper and lower power constraints defined by Equations (18) and (19) above are primarily aimed at frequency dynamic optimization on a short-term scale of seconds; their purpose is to prevent the energy storage converter from overloading or exceeding reverse charging limits during rapid power regulation. However, for the energy accumulation constraint represented by the energy storage unit's SOC, which spans the entire operating cycle, relying solely on scheduling by the upper-level energy management system at the minute scale is insufficient. Between two EMS scheduling commands, if the local optimizer continuously issues power commands that contradict the SOC state, this will lead to an integral saturation (wind-up phenomenon) effect and may even cause a sudden loss of frequency support.

To address this, this paper directly embeds SOC-aware hard constraints into the second-scale optimization model. Within each optimization step α, the recursive relationship for SOC is:

$$\mathrm{SOC}_j(k+1) = \mathrm{SOC}_j(k) - \frac{\eta_j \cdot P_{ess,j}(k) \cdot \alpha}{E_j^{cap}} \tag{20}$$

where η_j represents the charge-discharge efficiency and E_j^{cap} represents the rated capacity of the jth energy storage unit. Based on this recursive relationship, when the SOC crosses the safety threshold, the optimizer will enforce the following constraints:

$$\begin{cases} P_{ess,j} \geq 0, & \text{if } \mathrm{SOC}_j \leq \mathrm{SOC}_j^{\min} \\ P_{ess,j} \leq 0, & \text{if } \mathrm{SOC}_j \geq \mathrm{SOC}_j^{\max} \end{cases} \tag{21}$$

The introduction of Equation (21) ensures that when the SOC of an energy storage unit reaches a preset safety threshold, the local optimizer automatically cuts off or reverses the charging/discharging direction within seconds, thereby preventing the wind-up effect at its source. Simultaneously, this constrained state is fed back to the leader optimization layer, causing it to automatically reduce the weight of frequency regulation reliance on that unit in subsequent game-theoretic decisions, thereby ensuring the continuity and reliability of system frequency support.

In addition, frequency constraints in the power grid must also be taken into account. We use the oscillation equations of a synchronous generator to describe the frequency dynamics of the power grid:

$$2H_{sys}\frac{\mathrm{d}\Delta\omega_s}{\mathrm{d}t} + D_{sys}\Delta\omega_s = \Delta P_{gen} + \Delta P_{ess} - \Delta P_{load} \tag{22}$$

Here, H_{sys} is the system's equivalent inertia time constant, D_{sys} is the system's equivalent damping coefficient, ΔP_{gen} is the change in synchronous generator output, ΔP_{ess} is the total change in VSG output, and ΔP_{load} is the change in load. The local frequency $\omega_{s,i}$ at node i is obtained by measuring the phase of the PCC voltage via a phase-locked loop (PLL), and its dynamic response can be approximated as a first-order inertial element:

$$\Delta\omega_{s,i}(s) = \frac{1}{1+sT_{pll}}\Delta\omega_{sys}(s) \tag{23}$$

In the equation, T_{pll} represents the measurement time constant of the PLL. At each time step α, the optimization algorithm predicts the frequency response within a short future time window based on the current system state, thereby achieving forward-looking optimization control.

3.2. Gradient-Based Leader–Follower Game Approach

The leader–follower game is a non-cooperative game typically used to model decision-making interactions between a leader and one or more followers [38,39]. The leader makes the initial decision, and then the follower selects its optimal strategy based on the leader's action. The leader then anticipates the follower's response and formulates the optimal decision accordingly. The procedural flowchart of this algorithm is illustrated in Figure 5.

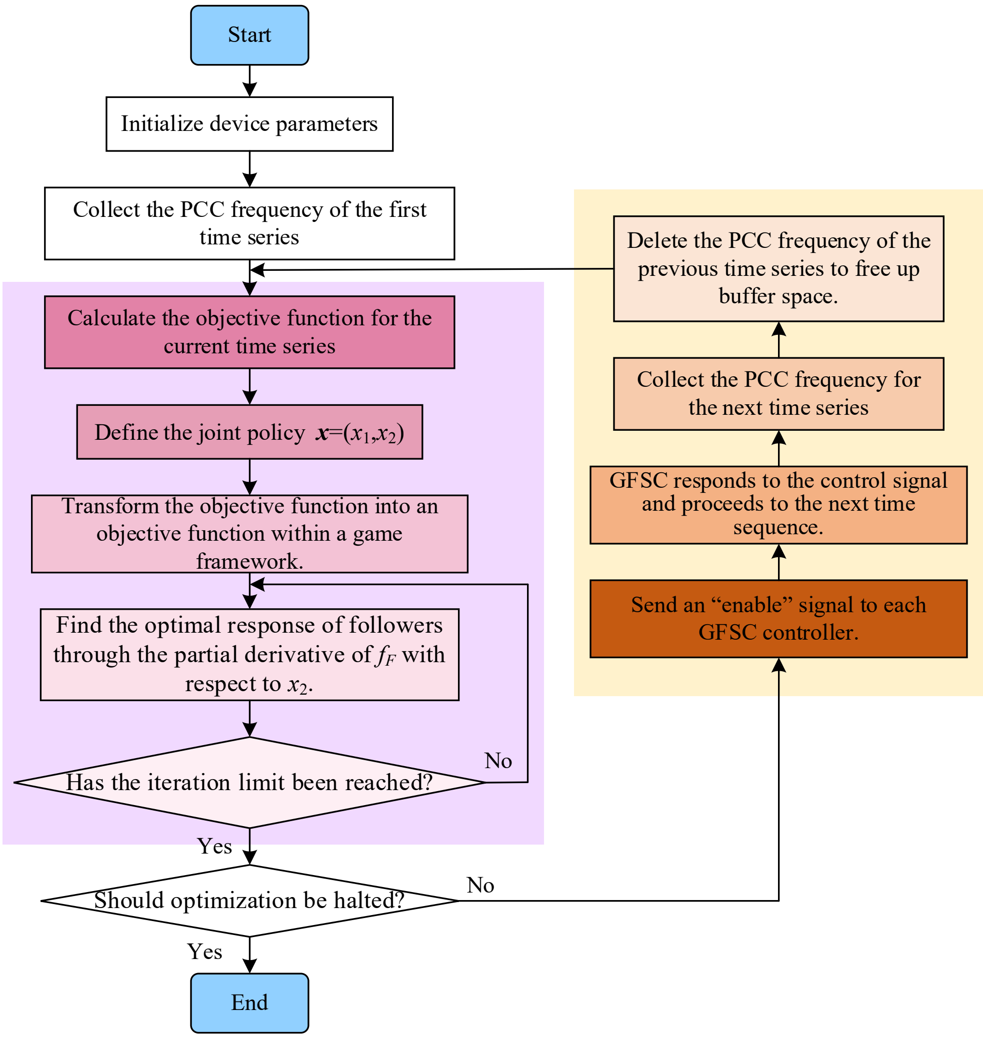

Figure 5. Flowchart of the gradient-based leader–follower game algorithm.

In this study, a leader–follower game framework is employed to coordinate active power allocation among multiple energy storage VSGs. The central optimizer is designated as the leader, with its decision variable being the system frequency deviation reference adjustment. The local controllers of each energy storage VSG are set as followers, with their decision variables being the respective active power output adjustments.

Assume the leader's strategy is x_1, representing the overall frequency deviation. The follower's strategy is x_2, representing the active power compensation value for each GFM-ESS. The joint strategy is defined as $\boldsymbol{x} = (x_1, x_2)$. The objective is to minimize the objective functions $f_{\mathrm{L}}(\boldsymbol{x})$ and $f_{\mathrm{F}}(\boldsymbol{x})$ for the leader and follower respectively.

Leader objective function $f_{\mathrm{L}}(\boldsymbol{x})$: The leader aims to minimize the frequency deviation across the entire system, namely:

$$f_L(x_1, x_2) = \min f^{\alpha} \tag{24}$$

Follower objective function $f_{\mathrm{F},j}(\boldsymbol{x})$: Each follower (the jth VSG) seeks to minimize its own control cost whilst adhering to the leader's strategy. This cost encompasses both the deviation from the leader's command and the rate of change in its own power output, defined as:

$$f_{F,j}(x_1, x_2) = \min\left[\left(\Delta P_j - \Delta P_{j,cmd}\right)^2 + \lambda\left(\frac{d\Delta P_j}{dt}\right)^2\right] \quad (25)$$

Here, ΔP_{cmd} denotes the active power command derived from the leader's strategy x_1, and λ is a weighting coefficient.

The optimal response of a follower is to minimize its local objective function $f_{\mathrm{F}j}(\boldsymbol{x})$. The leader then updates its strategy $\boldsymbol{x}$ based on all followers' responses to minimize the global frequency deviation $f_{\mathrm{L}}(\boldsymbol{x})$. The optimal response function for the follower can be derived from the partial derivative of f_{F} with respect to x_2:

$$x_2^*(x_1) = \arg\left[\min_{x_2} f_{\mathrm{F}}(x_1, x_2)\right] \quad (26)$$

Subsequently, the leader makes their own decision after considering the follower's response. The leader knows that the follower will select the optimal response function based on their own choice x_1. Therefore, the leader's objective is to minimize their own objective function:

$$\nabla f_{\mathrm{L}}(x_1, x_2^*(x_1)) = \frac{\partial f_{\mathrm{L}}(\boldsymbol{x})}{\partial x_1} + \nabla x_2^*(x_1)\frac{\partial f_{\mathrm{L}}(\boldsymbol{x})}{\partial x_2} \quad (27)$$

among which:

$$\nabla x_2^*(x_1) = \frac{\partial^2 f_{\mathrm{F}}(x_1, x_2)}{\partial x_2^2} + \frac{\partial^2 f_{\mathrm{F}}(x_1, x_2)}{\partial x_1 \partial x_2} \quad (28)$$

Calculation of the Leader's Gradient: The leader's optimization problem can be formulated as a two-level optimization subject to the constraint of the followers' optimal responses [40]:

$$\min_{x_1} f_L(x_1, R(x_1)) \quad (29)$$

where $R(x_1) = [R_1(x_1), R_2(x_1), \ldots, R_{\mathrm{n}}(x_1)]^{\mathrm{T}}$ is the vector of the followers' optimal responses, given by Equation (24). The gradient of the leader's objective function f_L with respect to the strategy x_1 can be expressed as:

$$\nabla_{x_1} f_L = \frac{\partial f_L}{\partial x_1} + \sum_{j=1}^{n} \frac{\partial f_L}{\partial R_j}\frac{\partial R_j}{\partial x_1} \quad (30)$$

Derivative of the follower's response function: From Equation (24), it follows that the optimal response function $R_j(x_1)$ of the jth follower satisfies the first-order optimality condition:

$$\frac{\partial f_{F,j}}{\partial x_{2,j}}(x_1, R_j(x_1)) = 0 \quad (31)$$

Differentiating both sides of Equation (29) with respect to x_1 yields:

$$\frac{\partial^2 f_{F,j}}{\partial x_{2,j}\partial x_2} + \frac{\partial^2 f_{F,j}}{\partial x_{2,j}^2}\frac{\mathrm{d}R_j}{\mathrm{d}x_1} = 0 \quad (32)$$

From this, we obtain:

$$\frac{\mathrm{d}R_j}{\mathrm{d}x_1} = -\left(\frac{\partial^2 f_{F,j}}{\partial x_{2,j}^2}\right)^{-1}\frac{\partial^2 f_{F,j}}{\partial x_{2,j}\partial x_2} \quad (33)$$

Numerical implementation of the gradient: Since the relationship between f_L and x_1 is determined by complex grid dynamics, its analytical gradient is difficult to obtain directly. Therefore, this paper employs the central difference method to numerically approximate the leader's gradient:

$$\nabla_{x_1} f_L \approx \frac{f_L(x_1+\varepsilon, R(x_1+\varepsilon)) - f_L(x_1-\varepsilon, R(x_1-\varepsilon))}{2\varepsilon} \tag{34}$$

where ε is the perturbation step size for numerical differentiation, set to 10^{-4}. For each perturbed point $(x_1 \pm \varepsilon)$, the follower's optimal response $R(x_1 \pm \varepsilon)$ must be recalculated, which is achieved by solving Equation (24).

It should be noted that this gradient-based iterative solution process typically converges rapidly to a local optimum when the objective function is convex and the step size is appropriately chosen. In Section 4, multi-scenario simulations will be used to verify the convergence of this algorithm within the range of system parameters under study, while a rigorous theoretical proof of its global convergence will be a focus of future research.

3.3. Active Power Branch Compensation Control

Based on the master–slave game optimization model, each optimization cycle yields a set of optimal active power control commands ΔP_{cmd} for the energy storage VSG. However, applying these step commands directly to the VSG control system would introduce high-frequency noise and system disturbances, potentially leading to voltage and current distortion or even triggering protective actions. To address this issue, this paper introduces a Tracking Differentiator (TD) to achieve a smooth transition from discrete optimization commands to continuous compensation signals. The TD structure adopts the Fastest Discrete TD, whose discrete form is as follows:

$$\begin{cases} x_1(k+1) = x_1(k) + hx_2(k) \\ x_2(k+1) = x_2(k) + h \cdot \text{fhan}(x_1(k) - v(k), x_2(k), r, h_0) \end{cases} \tag{35}$$

where $v(k)$ is the input signal (optimized command ΔP_{cmd}), x1 is the tracking output of the input signal (i.e., the final compensation signal ΔP_{comp} applied to the VSG), x_2 is the derivative of x_1, h is the simulation step size, r is the speed factor determining the tracking rate, h_0 is the filtering factor for noise suppression, and fhan(x_1, x_2, r, h) is the fastest control synthesis function, defined as:

$$\text{fhan}(x_1, x_2, r, h) = -\begin{cases} r \cdot \text{sign}(a), & |a| > r \cdot h \\ r \cdot \frac{a}{d}, & |a| \le r \cdot h \end{cases} \tag{36}$$

$$\begin{cases} a = \begin{cases} x_2 + \frac{a_0 + r \cdot h}{2} \cdot \text{sign}(y), & |y| > r \cdot h^2 \\ x_2 + \frac{y}{h}, & |y| \le r \cdot h^2 \end{cases} \\ y = x_1 + h \cdot x_2, a_0 = \sqrt{r^2 \cdot h^2 + 8r|y|} \end{cases} \tag{37}$$

The specific control block diagram and flowchart for active power branch compensation control are shown in Figure 6.

The control "enable" signal is converted by the TD into a continuous analogue signal rather than a step function updated at the optimized cycle frequency. The optimized VSG achieves continuous frequency optimization by compensating for deviations in the active power branch.

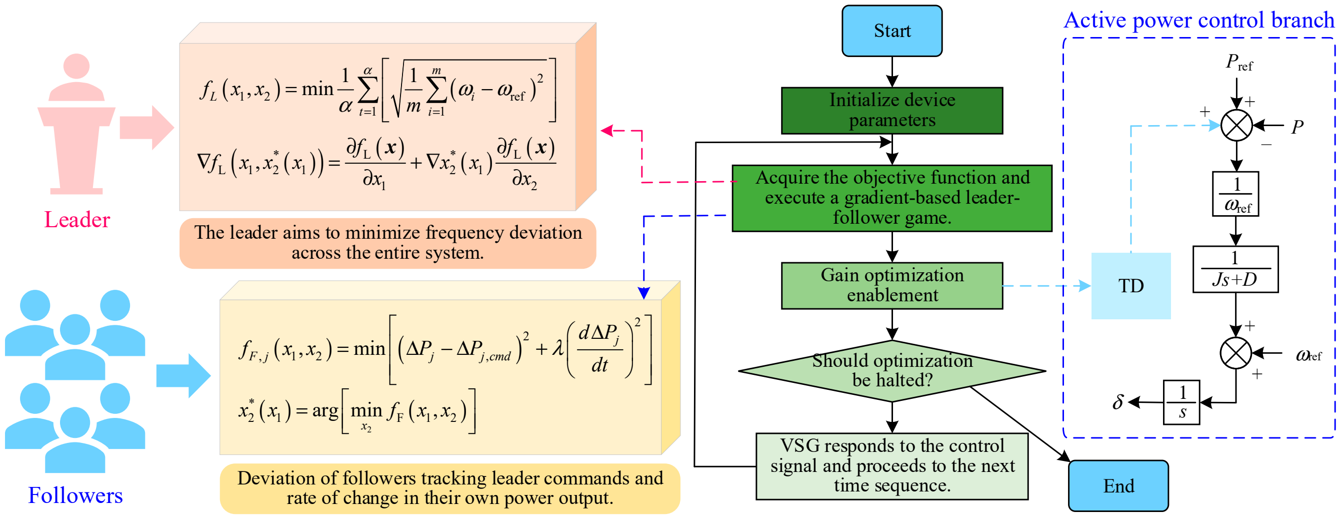

Figure 6. Control flowchart of active power compensation.

4. Simulation Verification

4.1. Simulation Settings

This paper employs a modified IEEE 33-node network to validate the efficacy and superiority of the proposed methodology [41]. It is based on IEEE-33, with six VSG energy storage units added and connected to the node via a 0.38/10 kV autotransformer. The original AC power source in the IEEE 33-node system has been replaced with a 6 MW synchronous generator. The system's equivalent inertia time constant is H_{sys} = 2 s, and the system's equivalent damping coefficient is D_{sys} = 0.5. The improved IEEE-33 network structure is shown in Figure 7. The maximum capacity and initial SOC of the energy storage devices are detailed in Table 1.

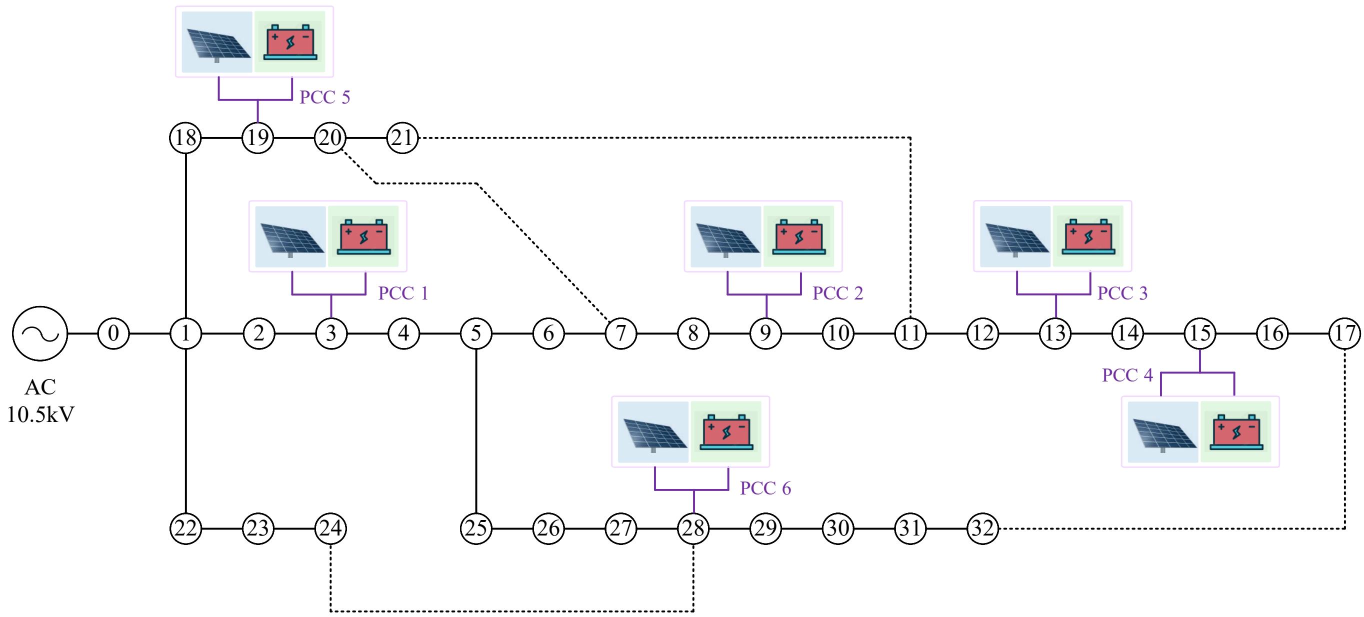

Figure 7. Improved IEEE-33 node network.

The model was constructed in MATLAB 2023b/Simulink, with the gradient-based leader–follower game optimization model implemented using a MATLAB Function block. Frequency data was obtained by calculating the PCC voltage values acquired via the phase-locked loop. The control parameters for the energy storage VSG are detailed in Table 2.

Additionally, the line impedance information for the energy storage VSG's connection to the IEEE-33 grid is presented in Table 3.

Table 1. Maximum capacity and initial SOC of energy storage devices.

PCC Number	Maximum Capacity (kWh)	Initial SOC (%)
1	100	30
2	200	80
3	200	80
4	150	80
5	100	30
6	150	50

Table 2. Control parameters of energy storage VSGs.

Parameters	Value	Parameters	Value
J	0.2 kg·m^2	D	100 W·s/rad
K_{qu}	0.1 V/Var	P_{ref}	60 kW
Q_{ref}	10 kVar	ω_{ref}	100π rad/s
U_{ref}	311 V		

Table 3. Impedance of energy storage VSG access node.

PCC Number	Line Resistance (Ω)	Line Reactance (Ω)
1	0.731328	0.172987
2	0.966316	0.228571
3	0.240656	0.056924
4	1.01712	0.240588
5	0.288132	0.068154
6	0.79586	0.188252

The GCC access impedance for new energy equipment matched with GFM-ESSs is shown in Table 4, with control parameters detailed in Table 5.

Table 4. Impedance at the connection point for new energy equipment.

PCC Number	Line Resistance (Ω)	Line Reactance (Ω)
1	0.65498	0.14906
2	1.01451	0.23089
3	0.83789	0.19069
4	1.02321	0.23287
5	0.73015	0.16617
6	1.00181	0.22799

Table 5. GCC Control Parameters for New Energy Equipment.

Parameters	Value	Parameters	Value
$P_{r,ref}$	120 kW	$Q_{r,ref}$	50 kVar
k_{pP}	0.1 A/W	k_{iP}	10 A/W
k_{pQ}	0.1 A/Var	k_{iQ}	10 A/Var
k_{pi}	1 Ω	k_{ii}	20 Ω
$k_{p,pll}$	180 Hz/V	$k_{i,pll}$	3200 Hz/V

4.2. Simulation Results

Assuming the dashed line in Figure 7 is connected at the 60th second of simulation to simulate a change in grid state, the optimized strategy described herein is implemented in the enhanced IEEE-33 node system. We implemented the optimization strategy described in this paper in the modified IEEE-33-node system. We first verified the active power injection of each GFM-ESS, as this is a prerequisite for frequency stability in a grid-forming control system. We present the active power waveforms of GFM-ESS units 1 and 2, as shown in Figure 8. We can confirm that each GFM-ESS injects stable active power into the grid; therefore, we present the frequency waveforms of each PCC in Figure 9. The time origin for each window is the 30th second of simulation. As shown in Figure 9, the unoptimized case (Traditional VSG control) exhibits noticeable high-frequency oscillations at the PCCs. In contrast, the proposed optimization method significantly suppresses these oscillations, demonstrating its effectiveness in mitigating frequency fluctuations. Upon further examination of Figure 8, it is evident that the amplitude of the oscillation in the optimized PCC frequency has been significantly suppressed. Concurrently, it is evident that during grid disturbances, the optimized PCC frequency demonstrates a significantly reduced response time and markedly diminished frequency fluctuation magnitude. Based on the simulation results, we have also confirmed that the algorithm's output exhibits global convergence.

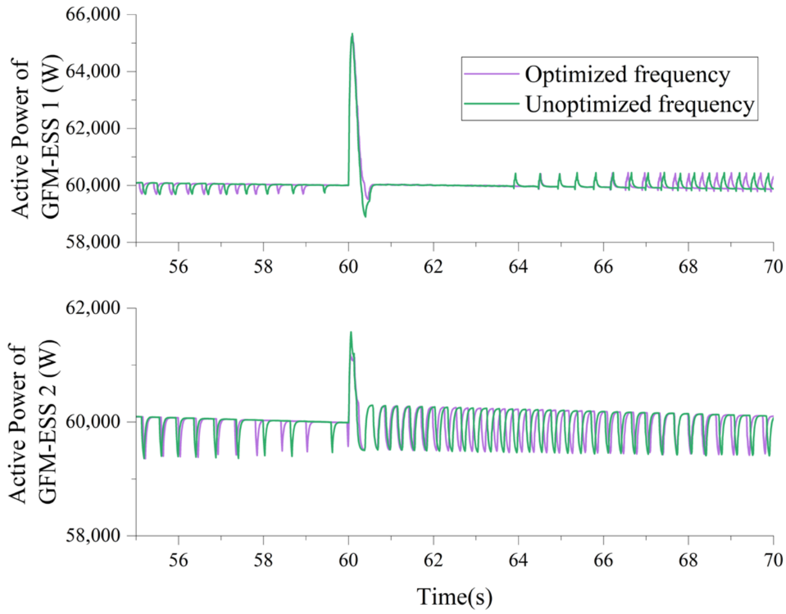

Figure 8. Active power waveforms for GFM-ESS units numbered 1 and 2.

To quantify the results under grid fluctuation conditions, the frequency response time is defined as the duration from the onset of fluctuation to reaching 90% of steady-state; while the frequency fluctuation value is defined as the absolute error between the maximum frequency during the fluctuation and the reference frequency value. The quantified comparisons of frequency response time and frequency fluctuation value are shown in Figures 10 and 11. The comparison reveals that the optimized frequency response time is reduced by 25.8% to 66.3% compared to the pre-optimized case. Concurrently, the frequency fluctuation value is optimized by 7.21% to 86.1%.

Furthermore, to statistically analyze the frequency distribution across all PCC points, the frequency data collected during 300 s of steady-state operation is presented in Figure 12. As illustrated in Figure 12, the optimized frequency distribution exhibits greater concentration, with a significantly reduced standard deviation compared to the pre-optimization state. This provides statistical evidence of the method's effectiveness in enhancing frequency steady-state performance. Consequently, the optimized PCC frequency distribution is markedly more concentrated, resulting in substantially improved steady-state frequency performance.

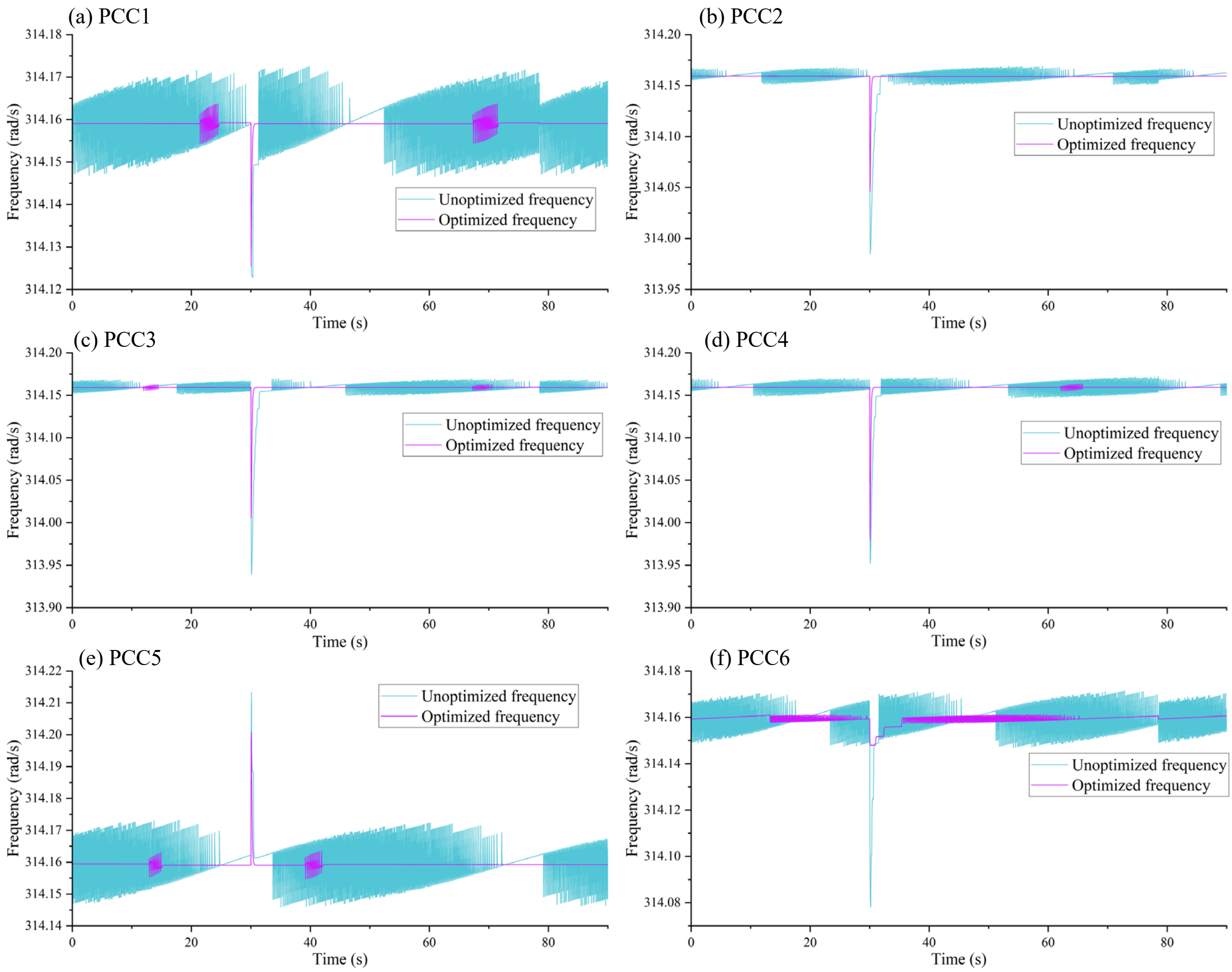

Figure 9. Frequency waveforms of all PCCs.

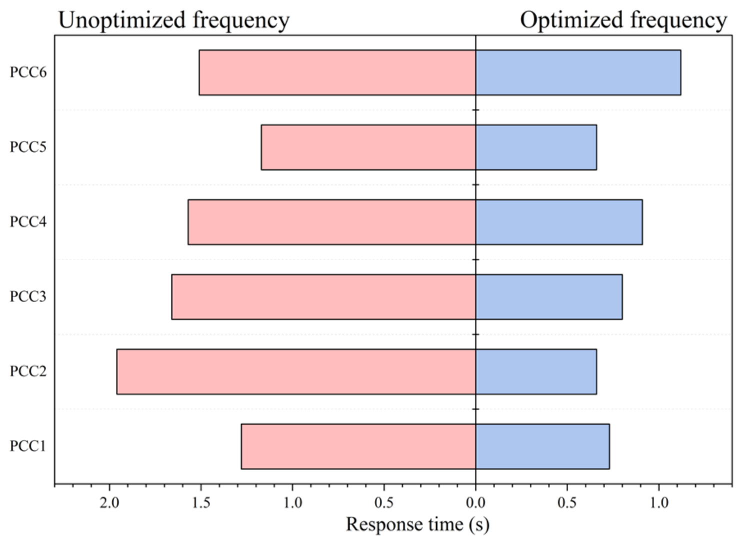

Figure 10. Frequency response time comparison.

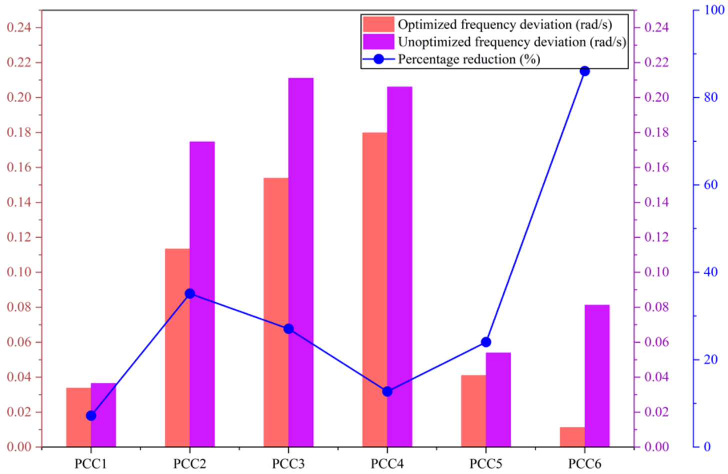

Figure 11. Comparison of frequency fluctuation values.

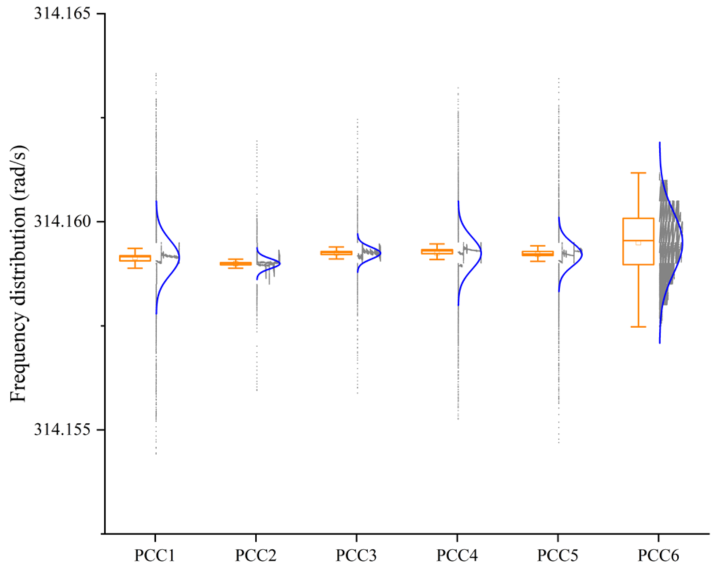

(**a**) Optimized frequency distribution

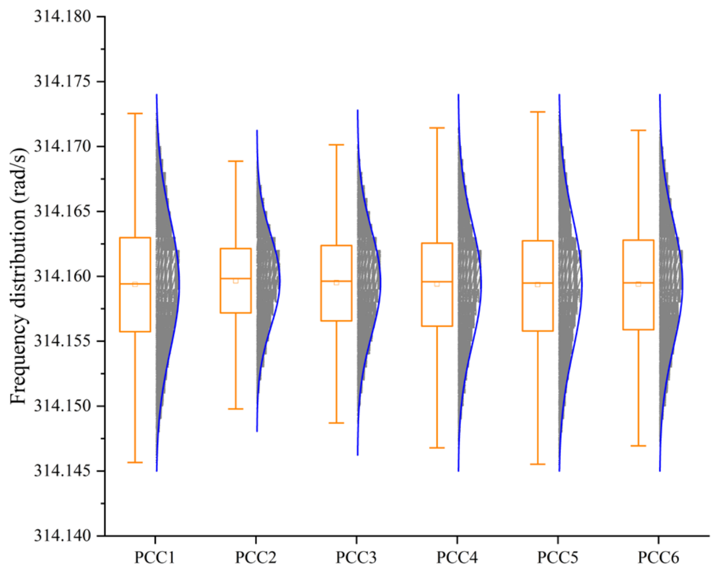

(**b**) Unoptimized frequency distribution

Figure 12. Statistical results of frequency data.

Finally, we also need to verify the frequency improvements at other nodes. We collected three-phase voltage data from all nodes and used the instantaneous phase angle difference method to extract the frequencies at all nodes before and after the disturbance. Based on the frequency samples, we calculated the frequency fluctuation values before and after optimization and compared them, as shown in Figure 13.

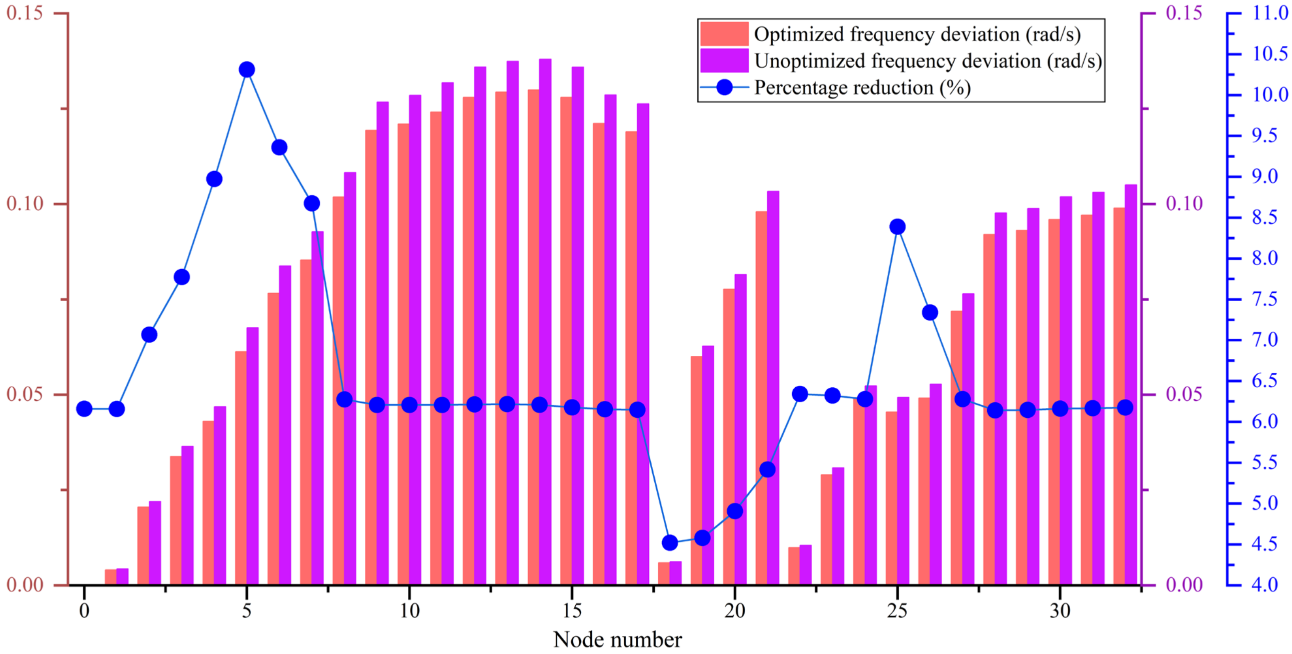

Figure 13. Comparison of frequency fluctuation values for all nodes.

As shown in Figure 13, the frequency fluctuation values for all nodes have improved to varying degrees. Additionally, the PCC data corresponding to the GFM-ESS differs slightly from that in Figure 11. This is because the frequency data in Figure 11 was obtained via phase-locked loop sampling; the difference in data is due to the different sampling methods and falls within an acceptable error range.

In summary, compared with conventional droop control and fixed-parameter VSGs, the method proposed herein demonstrates distinct advantages in response speed, oscillation suppression, and multi-machine coordination. This optimization approach achieves substantial reductions in both response time and rate of frequency change by controlling the energy storage VSG, thereby ensuring the system's frequency stability.

4.3. Computational Complexity and Scalability Analysis

Since the method proposed in this paper is designed for "fast" quadratic control at the second level, its computational scalability in large-scale systems must be demonstrated. Under the current centralized master–slave game framework, the leader's gradient is computed using the central difference method; each iteration requires applying two perturbations to the leader's strategy and independently solving the optimal response function for each follower. Let n denote the number of VSG units. The theoretical computational complexity per iteration is limited by the number of follower problems to be solved, reaching $O(n^2)$ in the worst case. However, since the optimal response functions of the followers in this application have closed-form solutions and involve only lightweight algebraic operations, the actual computational burden is far lower than the theoretical worst-case estimate.

To empirically verify the algorithm's real-time feasibility, this paper extracts the core optimization module and conducts offline scalability tests. The test platform is consistent with the simulation environment described in Section 4. By constructing synthetic frequency-sampled data, the average time required for a single optimization is measured point-by-point within the range of $n = 2$ to $n = 20$. Each test point is independently repeated multiple times, and the mean and standard deviation are recorded; the results are shown in Figure 14. The test results indicate that, within the range of $n \leq 20$, the computation time for a single optimization increases approximately linearly with the number of elements, rather than following the theoretical worst-case quadratic relationship. This linear trend can be attributed to the fact that the dominant computational overhead of the current algorithm is concentrated in the element-by-element perturbations and vector operations within the leader gradient loop, while the closed-form follower response function incurs nearly constant time per invocation. Under the six-machine configuration deployed in this paper, the average time per optimization cycle is only 3 ms, which is far less than the 1-s optimization cycle and meets real-time operation requirements. Even when extrapolated to a scenario with $n = 20$ machines, the estimated runtime remains well below the sampling threshold. This near-linear computational growth characteristic provides strong algorithmic support for the "fast" optimization positioning of the method described in this paper and offers a basis for its feasibility in larger-scale distributed grid-connected energy storage systems.

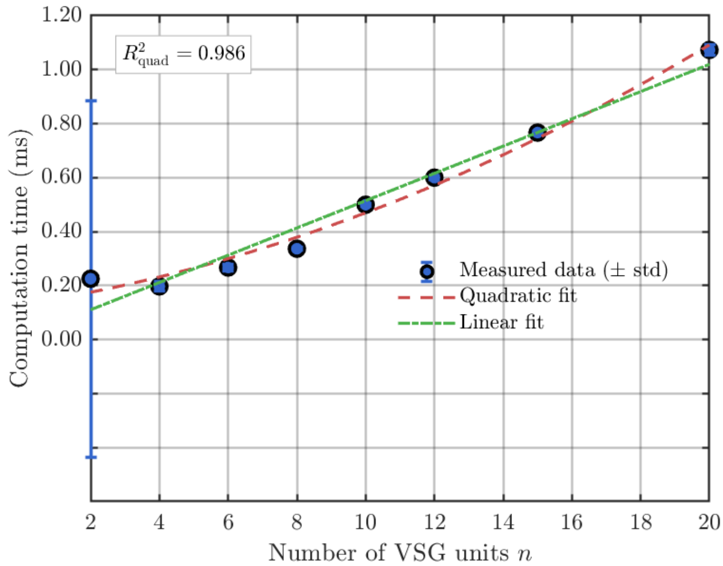

Figure 14. Results of the short-term optimization complexity analysis.

As shown in Figure 14, the execution time is approximately 1.1 ms for $n = 2$, 3.0 ms for $n = 6$, 5.8 ms for $n = 12$, and 9.2 ms for $n = 20$. The rate of increase in computation time with respect to n is nearly constant. This is due to the closed-form analytical solution of the follower's response function in this application—the time taken per call is constant for all values of n. Therefore, the actual bottleneck of the algorithm lies in the $O(n)$ element-wise perturbations within the leader's gradient loop, which exhibit near-linear growth rather than the theoretical worst-case $O(n^2)$ behavior.

4.4. Comparative Analysis

This paper employs a centralized frequency optimization control method. However, since most current frequency optimization control strategies tend to be distributed, we introduce two distributed optimization control methods developed by other researchers for comparative analysis with our method. Comparison 1: Constructing an active power feedforward channel that detects changes in active power via a differential element to reduce frequency fluctuations. This method is commonly referred to as Transient Damping

Control (TDCC). Comparison 2: Constructing a Distributed Adaptive Damping Control (SADA) algorithm that optimizes the controller's output based on its own state. We incorporate these two comparison strategies into the GFM-ESS environment described in this paper and validate them on the IEEE-33 node network. It is worth noting that we constructed the control models for TDCC and SADA based on Refs. [42,43], with parameter configurations identical to those in the original papers. We use the frequency fluctuation value when the system is subjected to disturbances as a quantitative metric, as shown in Figure 15.

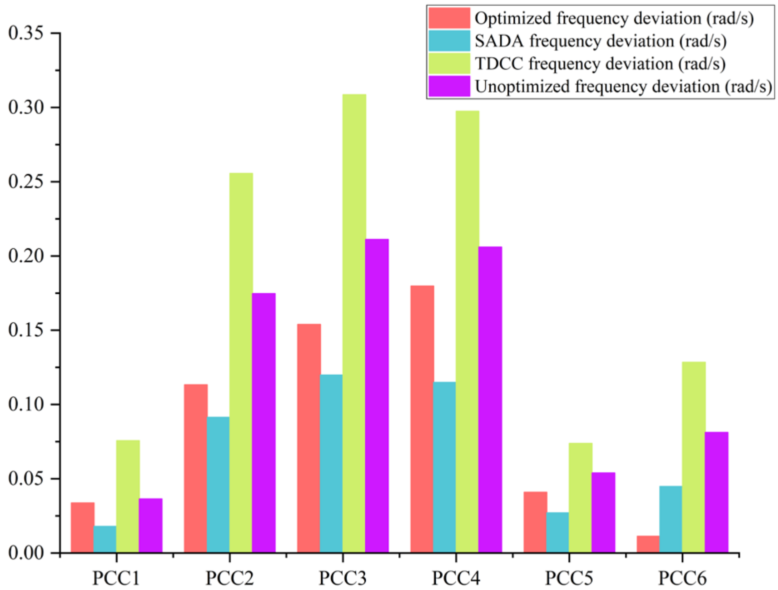

Figure 15. Comparative Analysis of Frequency Fluctuation Values.

Based on the comparative analysis results, it can be observed that SADA exhibits the smallest frequency fluctuation; however, SADA reduces the frequency fluctuation by increasing damping instantaneously upon disturbance, which results in prolonged response time. Furthermore, while TDCC exhibits the highest frequency fluctuation, it also has the shortest response time; however, excessive frequency fluctuation may lead to frequency instability. In contrast, the strategy proposed in this paper achieves a relatively better balance between frequency fluctuation suppression and response time improvement, making it more suitable for distributed GFM-ESS environments.

5. Conclusions, Limitations, and Recommendations

5.1. Conclusions of This Article

This paper aims to enhance the frequency stability of grid-forming energy storage systems when integrated into distribution networks. This paper proposes a fast dynamic optimization method for the active power–frequency control loop, specifically designed for VSG-based energy storage integration. Based on the research findings, the following conclusions are drawn: A coupling relationship has been established between the equivalent voltage and electrical angle of the VSG, derived from its external power characteristics, and its active and reactive power outputs. Building upon this, a fast and continuous optimization model is formulated, with the objective function set to minimize the frequency deviation at the PCC node. This model employs a gradient-based leader–follower game approach to achieve efficient optimization at short time scales, demonstrating excellent performance. Finally, simulation experiments on the IEEE-33 node network further validate the effectiveness of this method in reducing frequency deviation. Simulation results demonstrate that this optimization strategy substantially reduces frequency dispersion and mitigates frequency fluctuations. Moreover, under grid disturbances, the method reduces frequency response time by 25.8% to 66.3% and decreases the amplitude of frequency fluctuations by 7.21% to 86.1%, significantly enhancing the system's dynamic frequency response performance.

5.2. Limitations

Although the frequency optimization method based on gradient master–slave games proposed in this paper has demonstrated good performance in simulations, it still has certain limitations. First, both the decoupled control strategy and the game-theoretic optimization model rely on a small-signal linearization approximation of the system near a steady-state operating point. When the system encounters large-signal disturbances such as short-circuit faults or the connection/disconnection of large-capacity units, the model accuracy and control performance may deteriorate. Second, this method employs a centralized leader optimizer for global coordination. While this approach is easy to implement, it carries a single-point-of-failure risk and places high demands on the reliability of the communication network. Furthermore, as the number of connected VSG energy storage units increases, the computational burden of the optimization algorithm will grow superlinearly, placing higher demands on the real-time computing capabilities of the hardware control platform. These limitations will be the focus of attention and improvement in future research.

5.3. Recommendations for Future Research

To address the aforementioned limitations, we suggest that future research focus on the following areas:

(1). Investigate robust distributed optimization architectures designed for large-signal disturbances and weak communication environments, such as replacing the centralized leader–follower structure with fully distributed non-cooperative game algorithms to enhance system scalability and resilience.

(2). Introduce a model predictive control framework to integrate the long-term SOC constraints of energy storage units with short-term frequency regulation objectives into a rolling optimization model, thereby achieving coordinated control across multiple time scales.

(3). Explore intelligent optimization methods based on data-driven or adaptive dynamic programming to reduce the reliance of control strategies on precise mathematical system models and enhance their adaptability under complex operating conditions.

Author Contributions: Conceptualization, Y.G. (Yingjun Guo) and Y.Q.; Methodology, Y.G. (Yingjun Guo); Software, E.Z.; Validation, Y.Q.; Formal analysis, C.M. and Y.G. (Yanxun Guo); Investigation, E.Z.; Data curation, S.Z.; Writing—original draft, Y.Q.; Writing—review & editing, Y.G. (Yingjun Guo) and H.S.; Visualization, S.Z.; Project administration, C.M. and Y.G. (Yanxun Guo); Funding acquisition, H.S. All authors have read and agreed to the published version of the manuscript.

Funding: This work is supported by S&T Program of Hebei (23284502Z) and Hebei Natural Science Foundation (E2025208078).

Data Availability Statement: Data are contained within the article.

Conflicts of Interest: Author Chunxiao Mei was employed by Hebei Province Construction & Investment Group Co., Ltd. Authors Yanxu Guo and Shuo Zhang were employed by Suntien Green Energy Co., Ltd. Author Erhui Zhang was employed by HeBei Suntien New Energy Technology Co., Ltd. The remaining authors declare that the research was conducted in the absence of any commercial or financial relationships that could be construed as a potential conflict of interest.

References

1. Guo, Y.; Qi, Y.; Ge, L.; Hou, L.; Li, J.; Sun, H. Damping improvement of VSG with grid-forming driven by hybrid incremental feedback observer and transient vector compensation. *Proc. CSEE* **2024**, *44*, 1–13. (In Chinese)
2. Abomazid, A.M.; El-Taweel, N.A.; Farag, H.E.Z. Optimal energy management of hydrogen energy facility using integrated battery energy storage and solar photovoltaic systems. *IEEE Trans. Sustain. Energy* **2022**, *13*, 1457–1468. [CrossRef]
3. Liu, X.; Ma, T.; Tian, J.; Wei, Z.; Pan, T.; Wang, P. A novel double-layer active equalization scheme for lithium-ion batteries combining wireless power transfer. *Energy* **2024**, *291*, 130335. [CrossRef]
4. He, R.; Tian, K.; Ling, Z. Offline equalization control of modular multilevel converter-based battery energy storage system. *IEEE Trans. Ind. Electron.* **2024**, *71*, 9003–9012. [CrossRef]
5. Qi, Y.; Guo, Y.; Xie, P.; Sun, H. Joint Control of Storage Voltage Prediction and Grid-forming Converter using LSTM. In Proceedings of the 2025 IEEE International Conference on Power Systems and Smart Grid Technologies (PSSGT), Chongqing, China, 11–13 April 2025; pp. 280–287.
6. Ma, Y.; Tao, J.; Xu, Y.; Hu, H.; Liu, G.; Qin, T.; Fu, X.; Liu, R. Multi-objective control strategy for flexible multi-state switch based on supercapacitor energy storage under grid voltage imbalance. *High Volt. Eng.* **2024**, *50*, 5482–5494. (In Chinese)
7. Yuan, Q.; Bu, F.; Xie, X.; Xia, K. Improved model predictive voltage control for the NPC three-level dual three-phase PMSM based on vectors' classification. *Proc. CSEE* **2025**, *45*, 758–769. (In Chinese)
8. Guo, X.; Chen, G.; Zhao, L.; Ouyang, Q.; Kang, L. Systematic overview of equalization methods for battery energy storage systems. *J. Power Sources* **2025**, *640*, 236766. [CrossRef]
9. Tafizare, E.; Rahimi, M. Grid-following and grid-forming control modes of the rotor and grid sides converters for seamless and universal operation of the hybrid DFIG-wind/battery energy storage system in grid-connected and stand-alone conditions. *J. Energy Storage* **2024**, *104*, 114623. [CrossRef]
10. Me, S.P.; Ravanji, M.H.; Mansour, M.Z.; Zabihi, S.; Bahrani, B. Transient stability of paralleled virtual synchronous generator and grid-following inverter. *IEEE Trans. Smart Grid* **2023**, *14*, 4451–4466. [CrossRef]
11. Fu, Y.; Chen, Y.; Ji, L.; Li, S.; Yu, Z.; Li, Z.; Mi, Y. Low voltage ride-through control strategy of a grid-forming inverter considering power decoupling. *Power Syst. Prot. Control* **2024**, *52*, 1–13. (In Chinese)
12. Ge, P.; Xiao, F.; Tu, C.; Guo, Q.; Gao, J.; Song, Y. Transient stability enhancement control for VSG considering power angle stability and fault current limitation. *CSEE J. Power Energy Syst.* **2025**, *11*, 173–183.
13. Gao, S.; Dang, H.; Wang, L.; Du, Y.; Gao, X.; Lin, H.; Huangfu, Y. Large-Signal Stability Assessment for Islanded MGs With a Mix of Grid-Following and Grid-Forming Inverters: A Networked Oscillators-Based Approach. *IEEE Trans. Power Electron.* **2026**, *41*, 190–196. [CrossRef]
14. Sun, B.; Li, B.; Meng, F.; Wang, P.; Yu, X. Performance influence of auxiliary power batteries on hybrid energy storage system. *J. Energy Storage* **2025**, *114*, 115719. [CrossRef]
15. Lei, J.; Xiang, X.; Liu, B.; Li, W.; He, X. Quantitative and intuitive VSG transient analysis with the concept of damping area approximation. *IEEE Trans. Smart Grid* **2023**, *14*, 2477–2480. [CrossRef]
16. Yang, M.; Wang, Y.; Xiao, X.; Li, Y. A robust damping control for virtual synchronous generators based on energy reshaping. *IEEE Trans. Energy Convers.* **2023**, *38*, 2146–2159. [CrossRef]
17. Qu, Z.; Peng, J.C.-H.; Yang, H.; Srinivasan, D. Modeling and analysis of inner controls effects on damping and synchronizing torque components in VSG-controlled converter. *IEEE Trans. Energy Convers.* **2021**, *36*, 488–499. [CrossRef]
18. Lei, J.; Xiang, X.; Qu, Q.; Li, W.; He, X. The analysis and calculation of power angle transient characteristics in VSG control using parameter-perturbation-based averaging method. *IEEE Trans. Ind. Electron.* **2023**, *70*, 10249–10260. [CrossRef]
19. Wu, J.; Chen, X.; Zhang, D.; Yang, Z. Analysis and improvement strategies of grid-connected stability analysis and improvement strategy for grid-forming energy storage system in new energy access scene. *Proc. CSEE* **2024**, *44*, 9341–9354. (In Chinese)
20. Xu, C.; Zou, Z.; Chen, W.; Li, Q.; Lv, Z.; Zhang, S. Adaptive control method for grid-type energy storage systems aimed at improving transient stability. *Power Syst. Technol.* **2024**, *48*, 4658–4668. (In Chinese)
21. Xiong, L.; You, L.; Han, G.; Xiong, H.; Tian, M.; Xu, C. A method for tuning virtual impedance parameters in a network-type energy storage system based on single-voltage loop amplitude control using the Lyapunov energy function. *Power Syst. Prot. Control* **2025**, *53*, 30–41. (In Chinese)
22. Li, L.; Song, H.; Yan, Z.; Li, H.; Jin, P.; Zhao, J.; Qi, C. A two-stage robust optimization strategy for microgrids considering the grid-forming capability of energy storage and uncertainties of wind, photovoltaic, and load. *J. Energy Storage* **2025**, *140*, 118841. [CrossRef]
23. Mohanty, S.; Parida, S.M.; Rout, P.K.; Sahoo, B. Enhanced PLL-based power management algorithm for grid-connected hybrid systems with composite energy storage and electric vehicles. *J. Energy Storage* **2026**, *141*, 119284. [CrossRef]
24. Wang, X.; Ge, J.; Han, L.; Yu, Q.; Gao, Y.; Liu, Z. Theory and practice of grid-forming BESS supporting the construction of a new type of power system. *Power Syst. Prot. Control* **2023**, *51*, 172–179. (In Chinese)

25. Han, F.; Zhang, X.; Li, M.; Li, F.; Zhao, W. Stability control for grid-connected inverters based on hybrid-mode of grid-following and grid-forming. *IEEE Trans. Ind. Electron.* **2024**, *71*, 10750–10760. [CrossRef]
26. Zhang, H.; Xiang, W.; Lin, W.; Wen, J. Grid forming converters in renewable energy sources dominated power grid: Control strategy, stability, application, and challenges. *J. Mod. Power Syst. Clean Energy* **2021**, *9*, 1239–1256. [CrossRef]
27. Zhou, X.; Cheng, S.; Wu, X.; Rao, X. Influence of photovoltaic power plants based on VSG technology on low frequency oscillation of multi-machine power systems. *IEEE Trans. Power Deliv.* **2022**, *37*, 5376–5384. [CrossRef]
28. Hou, X.; Sun, Y.; Zhang, X.; Lu, J.; Wang, P.; Guerrero, J.M. Improvement of frequency regulation in VSG-based AC microgrid via adaptive virtual inertia. *IEEE Trans. Power Electron.* **2020**, *35*, 1589–1602. [CrossRef]
29. Fu, S.; Sun, Y.; Lin, J.; Chen, S.; Su, M. P/Q-ω/V Admittance Modeling and Oscillation Analysis for Multi-VSG Grid-Connected System. *IEEE Trans. Power Syst.* **2023**, *38*, 5849–5859. [CrossRef]
30. Zhang, K.; Shi, M.; Chen, X.; Shao, D.; Xu, Y.; Chen, Y. Interaction Modeling and Stability Analysis of Grid-Forming Energy Storage System Based on SISO Transfer Functions. *IEEE Trans. Sustain. Energy* **2025**, *16*, 573–587. [CrossRef]
31. Taul, M.G.; Wu, C.; Chou, S.-F.; Blaabjerg, F. Optimal controller design for transient stability enhancement of grid-following converters under weak-grid conditions. *IEEE Trans. Power Electron.* **2021**, *36*, 10251–10264. [CrossRef]
32. Pan, J.; Bao, Y.; Fu, X.; Xiao, J. Grid-forming control and analysis of novel storage energy integration system using four-level hybrid clamped converter. *J. Energy Storage* **2025**, *135*, 118269. [CrossRef]
33. Chen, X.; Huang, Z.; Yin, X.; Liang, Z. Control damping enhancement method of grid-forming battery energy storage system with diverse synchronization controls in asymmetrical grids. *J. Energy Storage* **2025**, *133*, 118028. [CrossRef]
34. Guo, Y.; Qi, Y.; Ge, L.; Hou, L.; Li, J.; Sun, H. Transient Compensation of Asymmetrical Line Faults in Multigrid-Forming VSG Systems. *IEEE Trans. Ind. Electron.* **2025**, *72*, 10085–10096. [CrossRef]
35. Shi, Q.; Dong, W.; Wang, G.; Ma, J.; Wang, C.; Guo, X. Grid Strength Assessment Method for Evaluating Small-Signal Synchronization Stability of Grid-Following and Grid-Forming Converters Integrated Systems. *J. Mod. Power Syst. Clean Energy* **2025**, *13*, 55–65. [CrossRef]
36. Xu, C.; Zou, Z.; Yang, J.; Wang, Z.; Chen, W.; Buticchi, G. Transient Stability Analysis and Enhancement of Grid-Forming and Grid-Following Converters. *IEEE J. Emerg. Sel. Top. Ind. Electron.* **2024**, *5*, 1396–1408. [CrossRef]
37. Yang, C.; Huang, L.; Xin, H.; Ju, P. Placing Grid-Forming Converters to Enhance Small Signal Stability of PLL-Integrated Power Systems. *IEEE Trans. Power Syst.* **2021**, *36*, 3563–3573. [CrossRef]
38. Chen, L.; Liu, N.; Li, C.; Wang, J. Peer-to-Peer Energy Sharing with Social Attributes: A Stochastic Leader–Follower Game Approach. *IEEE Trans. Ind. Inform.* **2021**, *17*, 2545–2556. [CrossRef]
39. Xu, G.; Chen, G.; Cheng, Z.; Hong, Y.; Qi, H. Consistency of Stackelberg and Nash Equilibria in Three-Player Leader-Follower Games. *IEEE Trans. Inf. Forensics Secur.* **2024**, *19*, 5330–5344. [CrossRef]
40. Wang, K.; Xu, L.; Perrault, A.; Reiter, M.K.; Tambe, M. Coordinating followers to reach better equilibria: End-to-end gradient descent for Stackelberg games. *Proc. AAAI Conf. Artif. Intell.* **2022**, *36*, 12345–12352. [CrossRef]
41. Dolatabadi, S.H.; Ghorbanian, M.; Siano, P.; Hatziargyriou, N.D. An enhanced IEEE 33 bus benchmark test system for distribution system studies. *IEEE Trans. Power Syst.* **2021**, *36*, 2565–2572. [CrossRef]
42. Wang, Z.; Chen, Y.; Li, X.; Xu, Y.; Luo, C.; Li, Q. Active Power Oscillation Suppression Based on Decentralized Transient Damping Control for Parallel Virtual Synchronous Generators. *IEEE Trans. Smart Grid* **2023**, *14*, 2582–2592. [CrossRef]
43. Fu, S.; Sun, Y.; Liu, Z.; Hou, X.; Han, H.; Su, M. Power oscillation suppression in multi-VSG grid with adaptive virtual inertia. *Int. J. Electr. Power Energy Syst.* **2022**, *135*, 107472. [CrossRef]